

Lattice and Continuum Modelling of a Bioactive Porous Tissue Scaffold

ANDREW L. KRAUSE, DMITRY BELIAEV, ROBERT A. VAN GORDER, SARAH L. WATERS

*Mathematical Institute, Andrew Wiles Building, University of Oxford
Radcliffe Observatory Quarter, Woodstock Rd, OX2 6GG, UK.*

[Received on XX XXX XXXX]

A contemporary procedure to grow artificial tissue is to seed cells onto a porous biomaterial scaffold and culture it within a perfusion bioreactor to facilitate the transport of nutrients to growing cells. Typical models of cell growth for tissue engineering applications make use of spatially homogeneous or spatially continuous equations to model cell growth, flow of culture medium, nutrient transport, and their interactions. The network structure of the physical porous scaffold is often incorporated through parameters in these models, either phenomenologically or through techniques like mathematical homogenization. We derive a model on a square grid lattice to demonstrate the importance of explicitly modelling the network structure of the porous scaffold, and compare results from this model with those from a modified continuum model from the literature. We capture two-way coupling between cell growth and fluid flow by allowing cells to block pores, and by allowing the shear stress of the fluid to affect cell growth and death. We explore a range of parameters for both models, and demonstrate quantitative and qualitative differences between predictions from each of these approaches, including spatial pattern formation and local oscillations in cell density present only in the lattice model. These differences suggest that for some parameter regimes, corresponding to specific cell types and scaffold geometries, the lattice model gives qualitatively different model predictions than typical continuum models. Our results inform model selection for bioactive porous tissue scaffolds, aiding in the development of successful tissue engineering experiments and eventually clinically successful technologies.

Keywords: tissue engineering, bioactive porous media, lattice and continuum models, model selection.

1. Introduction

Tissue engineering is a rapidly growing field seeking to apply techniques from a variety of disciplines to create tissues and organs. There is increased need for these technologies as patient transplant lists continue to grow, especially due to increased longevity (Beard et al., 2013). Despite significant progress in recent years, there is still a need to better understand the basic biological and physical aspects underpinning the engineering of artificially constructed tissues and organs in order to achieve widespread clinical success (Van Blitterswijk and Thomsen, 2008).

A contemporary strategy for *in vitro* tissue engineering is to seed cells onto a porous biomaterial scaffold which is placed inside a bioreactor where it is perfused with nutrient-rich culture medium (Cimetta et al., 2007; Glowacki et al., 1998; Kim et al., 2007). There is a large variation in cell types, scaffolds, and bioreactor geometries used to grow artificial tissues. Some cell types are mechano-sensitive and can be induced to proliferate, differentiate, or die in response to the local cellular mechanical environment, e.g. due to the fluid shear stress (Iskratsch et al., 2014; Riha et al., 2005). Some cells produce an extracellular matrix that is sufficiently dense to substantially affect the flow of culture medium through individual pores (Hossain et al., 2015). Understanding these fluid flow and cell growth interactions, and what roles they have in a tissue engineering experiment, is an important challenge.

Mathematical modelling plays a key role in underpinning experimental design, optimizing operat-

ing regimes, and predicting experimental outcomes (O'Dea et al., 2012). Mathematical models have also been used in lieu of costly and time-consuming experimental trials. There is a growing literature of models used to understand the interactions between fluid mechanical forces exerted on mechanosensitive cells, and the effect that cell growth has on the flow via pore-blocking. The simplest of these are spatially homogeneous models where ODEs are used to model the evolution of each phase, such as in Lemon et al. (2009).

To describe the spatial properties of artificial tissue growth, many macroscale continuum models for bioactive porous media have been proposed (O'Dea et al., 2012). These approaches are computationally much cheaper than a full simulation of flow within the underlying pore geometry and do not require detailed knowledge of the microstructure. Due to the complexity of growing tissue *in vitro*, and the wealth of biochemical and biophysical processes involved over a range of spatial and temporal scales, many different theoretical models exist in the literature (German and Madhally, 2016). These models result in partial differential equations for the dependent variables, such as cell density and fluid velocity, with constitutive assumptions describing the interactions between these variables.

Multiphase models account for multiple phases explicitly (e.g. fluid, scaffold, cells, etc). The governing equations are derived from conservation of mass and momentum for each phase, and interactions between the phases are captured via the specification of appropriate constitutive laws (O'Dea et al., 2010; Pearson et al., 2013). Alternatively, many models include the effect of cell growth on the fluid flow implicitly, by considering a cell density equation based on conservation of mass, and then prescribing the scaffold porosity to be a function of cell density (Coletti et al., 2006; Pohlmeier and Cummings, 2013; Pohlmeier et al., 2013; Shakeel et al., 2013). The flow of fluid through the porous scaffold is then governed by Darcy's law. In these macroscale approaches, constitutive assumptions relate microscale processes, such as cell growth, to macroscale parameters. In both cases, models have been derived that account for the influence of shear stress on cell growth. Additionally, homogenization techniques have been proposed to precisely capture the relationship between macroscopic parameters in these models, such as porosity, and growth and flow processes at the pore scale. We briefly give examples of each of these kinds of approaches below.

Pearson et al. (2016a,b, 2013, 2015) employed a multiphase approach to model fluid, scaffold, and cell phases within a hollow fibre bioreactor. This bioreactor design consists of parallel hollow permeable tubes which facilitate nutrient transport to the cells seeded in the extracapillary space surrounding the fibres. The small aspect ratio of the bioreactor was used to simplify this model, and the reduced system of governing equations were then solved numerically to gain insight into how to stimulate uniform cell growth throughout the scaffold. O'Dea et al. (2010) developed a three-phase model of cells, culture medium, and tissue scaffold with the aim of understanding the role of cell-cell and cell-scaffold interactions on tissue growth in a perfusion bioreactor. The focus was on mechanotransduction effects, such as the influence of fluid shear stress on the cell growth. Their analytical and simulation results gave insight into using experimental data to determine the dominant mechanical regulatory mechanisms within a cell population.

Coletti et al. (2006) proposed a model of nutrient transport, fluid flow, and cell growth in a tissue-engineering bioreactor which was used to investigate the effect of experimental protocols employed to overcome diffusion-limited transport, and to study adverse conditions that are observed experimentally, such as flow channeling along bioreactor walls. Accounting for both cell density-dependent permeability and mechanotransduction of shear stress by cells, Shakeel et al. (2013) investigated a generic model of nutrient transport and cell growth in a porous scaffold within a perfusion bioreactor. Cell proliferation and extracellular matrix deposition were assumed to decrease the local porosity, and hence permeability, of the scaffold, while moderate values of the shear stress were assumed to enhance both cell growth and

uptake of a generic nutrient by the cells. Pohlmeier and Cummings (2013) and Pohlmeier et al. (2013) used similar ideas to model other aspects of cell growth in perfusion bioreactors, including growth-factor driven haptotaxis.

Mathematical homogenization approaches have been proposed to upscale microscale features of the scaffold. Shipley et al. (2009) considered a model for fluid, glucose, and lactate transport in a microstructured porous medium. In this study, the variation of the effective permeability of the scaffold due to cell growth was not considered. Penta et al. (2014) developed a macroscopic model of a porous linearly elastic medium that accounted for mass exchange at the microscale between the phases due to accretion of the solid phase at the pore surface. O'Dea et al. (2015) considered the advection of a generic diffusible nutrient through a porous medium and derived macroscale equations accounting for microscale accretion of biomass at the pore surface due to the uptake of the nutrient.

In contrast to the spatially continuous models described above, network models have been used increasingly to describe porous media (Sahimi, 1993, 1994). McDougall (2002) developed a network model for angiogenesis induced by a nearby tumour, and investigated fluid flow through the resulting network structure. The results suggested that topological properties of the network, such as the number of loops, were crucial in understanding angiogenesis. Biofilms growing in porous media are another area where models of a dynamic pore network have been used. Thullner and Baveye (2008) proposed a lattice model of a porous medium, where growing biofilms clogged pores. Nutrients were also carried by the fluid, affecting the biofilm growth throughout the porous medium. Different constitutive assumptions relating pressure differences to flow rates in pore throats were explored to demonstrate global changes in hydraulic conductivity throughout the entire network. Stochastic network models, where the network topology and cell proliferation vary according to random processes, have also been explored to relate cell growth and fluid flow in the context of tissue engineering (Barbotteau et al., 2003; Mely and Mathiot, 2012; Tsimpanogiannis and Lichtner, 2012).

In contrast to the macroscale continuum and network models we have discussed, computational and algorithmic approaches have been employed to model various aspects of tissue engineering; see Geris (2013) for a comprehensive review. Nava et al. (2013) and Hossain et al. (2015) consider models directly accounting for the effects of fluid flow on cell growth that we are interested in here.

The pore and scaffold length scales in typical experiments with perfusion bioreactors can lead to scaffolds with relatively few pores, and it is unclear that macroscopic spatially continuous models will capture features present in small networks of pores. See Figure 6 of Cox et al. (2015) for an example of a porous scaffold with very few pores, and Loh and Choong (2013) and Vafai (2010) for general discussions of pore size, scaffold geometry, and transport phenomena in porous tissue scaffolds. Motivated by concerns with these spatially continuous modelling approaches, we propose a novel lattice model of a bioactive porous medium. We compare this to a typical continuum model, modified from Shakeel et al. (2013), to elucidate the different kinds of behaviour displayed by each modelling paradigm.

We consider the following biological system that captures many of the features encountered when engineering artificial tissues. We model a cell phase, which incorporates the extracellular matrix produced by the cells, and a fluid phase modelling the culture medium, which together saturate a two-dimensional porous scaffold. We consider model behaviours on the timescale of cell proliferation, focusing in particular on the role of shear stress on cell proliferation. In Shakeel et al. (2013) and Chapman et al. (2014) it was assumed that moderate levels of shear stress would enhance cell proliferation, but the detrimental effects of large shear stress were not considered. We are interested in the effects of high levels of shear stress not explored in those models, and assume that cells die if the local shear stress exceeds a certain threshold, either due to specific mechano-transduction mechanisms for apoptosis or due to detachment induced by the flow (McCoy et al., 2012). Finally, we assume that the culture

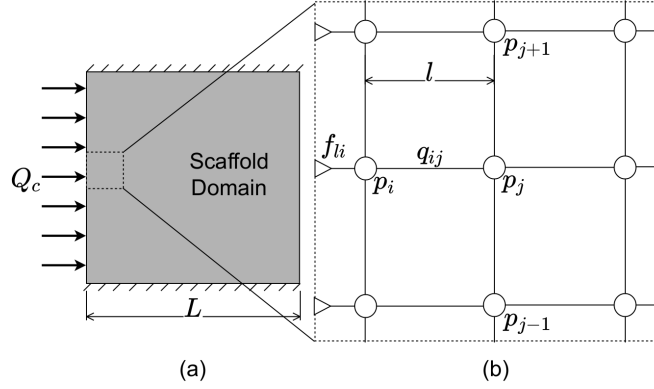


FIG. 1: A diagram of the scaffold domain (a) where fluid enters at a prescribed flow rate, Q_c , from the left and exits on the right side of the scaffold. The horizontal boundaries are impermeable. Enlarged (b) is the lattice structure of the scaffold, with fluid entering node i from the left boundary at a volumetric flow rate f_{li} . L denotes the size of the scaffold, l the length of an internal ‘pipe,’ p_i the pressure at node i , and q_{ij} the volumetric flow rate from node i to node j .

medium is pumped into the scaffold at a fixed flow rate, and that local increases in cell density decrease the local permeability of the scaffold.

In Section 2 we present our continuum and lattice modelling approaches, and discuss the physical and biological parameters. In Section 3 we compare results from these two models, primarily using numerical simulations. Finally in Section 4 we discuss the implications of our study for the successful modelling of porous media in tissue engineering applications.

2. Motivation and Modelling Frameworks

We consider a two dimensional rigid porous medium as a model of the tissue scaffold. For simplicity, we consider a square domain with side length L . The culture medium is an incompressible viscous Newtonian fluid, with dynamic viscosity μ . We assume that fluid is pumped at a constant flow rate Q_c (m^2s^{-1}) into the left side of the domain, and exits through the right side. We assume no fluid enters or leaves through the horizontal boundaries of the domain. See Figure 1(a) for a visualization of the domain. We assume that cells grow logistically, diffuse within the scaffold, and cannot leave the domain. We assume that cells will stop growing and will die if the shear stress exceeds a threshold value. Finally, the timescale of interest is that of cell proliferation, and so we neglect advection of the cells by the fluid.

2.1 Continuum Model of a Bioactive Porous Medium

We describe the square domain as spatially continuous with Cartesian coordinates $\mathbf{x}^* = (x^*, y^*) \in [0, L]^2$ (we use asterisks throughout to denote dimensional variables). We assume that the pore Reynolds number is small and neglect fluid inertia. We use Darcy’s Law to model flow through the scaffold (Bear, 1972), so that

$$\mathbf{u}^* = -\frac{k^*(x^*, y^*, N^*)}{\mu} \nabla^* p^* \quad \text{and} \quad \nabla^* \cdot \mathbf{u}^* = 0, \quad (2.1)$$

where \mathbf{u}^* is the Darcy velocity of the fluid, p^* is the fluid pressure, and $k^*(x^*, y^*, N^*)$ is the permeability of the scaffold which depends on the cell density N^* .

For ease of computation, we prescribe a pressure drop across the domain so that, along with no flux conditions at the horizontal boundaries, we impose

$$\mathbf{n} \cdot \mathbf{u}^* = 0 \text{ at } y^* = 0, L, \quad 0 \leq x^* \leq L, \quad (2.2)$$

$$p^* = p_0 \text{ at } x^* = 0, \quad 0 \leq y^* \leq L, \quad \text{and} \quad p^* = p_1 \text{ at } x^* = L, \quad 0 \leq y^* \leq L, \quad (2.3)$$

where p_0 is the upstream pressure, p_1 is the downstream pressure, and \mathbf{n} is the outward unit normal.

We use the linearity between pressure and the Darcy velocity to rescale the fluid variables to match the prescribed fluid flow rate through the scaffold. The total flow rate through the boundary at $x^* = 0$ is

$$Q_0^* = \int_0^L -\frac{k^*(0, y^*, N^*)}{\mu} \frac{\partial p^*}{\partial x^*} dy^*. \quad (2.4)$$

We define the rescaled Darcy velocity to be,

$$\mathbf{u}_r^* = \frac{Q_c}{Q_0^*} \mathbf{u}^*. \quad (2.5)$$

The cell density N^* is governed by the reaction-diffusion equation,

$$\frac{\partial N^*}{\partial t^*} = \beta \left(F_1(\sigma^*) N^* \left(1 - \frac{N^*}{N_c} \right) - F_2(\sigma^*) N^* \right) + D_n \nabla^{*2} N^*, \quad (2.6)$$

where t^* is time, N_c is the maximum cell density, β is the cell proliferation rate, D_n is the cell diffusion coefficient, σ^* is the fluid shear stress, and the dimensionless functions $F_1(\sigma^*)$ and $F_2(\sigma^*)$ capture the effect of fluid shear stress on growth and death. The terms on the right hand side correspond to logistic growth, cell death, and cell diffusion respectively. For simplicity we assume that β also captures the death rate due to high shear.

The no flux conditions for the cell density are,

$$\mathbf{n} \cdot \nabla N^* = 0 \text{ for } \mathbf{x} \in \partial[0, 1]^2, \quad (2.7)$$

where $\partial[0, 1]^2$ denotes the boundaries of the square domain. Finally we impose the following initial condition for cell density,

$$N^*(x^*, y^*, 0) = N_0^*(x^*, y^*), \quad (2.8)$$

where $N_0^*(x^*, y^*)$ is the initial scaffold seeding density.

We now specify how the scaffold permeability k^* appearing in Equation (2.1) depends on the cell density N^* . Following Coletti et al. (2006), we write the porosity as

$$\hat{\phi}(N^*) = \phi_0(1 - \nu N^*), \quad (2.9)$$

where ϕ_0 is the volume fraction of pore space in the scaffold without cells, and ν is the volume of pore space occupied by an individual cell. We require that $\nu N_c \leq 1$ so that under the bounded dynamics of Equation (2.6), $0 \leq \hat{\phi}(N^*) \leq \phi_0$ for all $N^* \leq N_c$.

We follow Shakeel et al. (2013) and relate the cell-dependent porosity to the scaffold permeability via

$$k^*(N^*) = k_0 \hat{\phi}(N^*)^3, \quad (2.10)$$

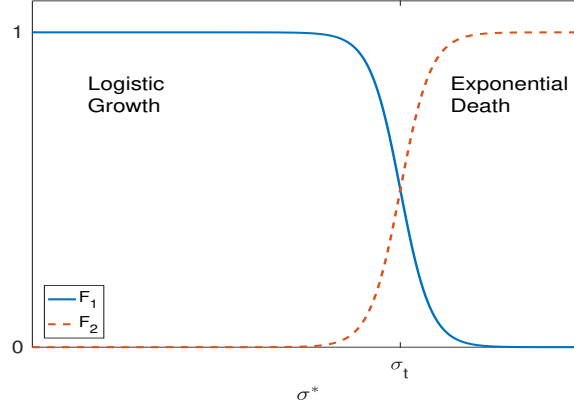


FIG. 2: Plots of the shear stress functions, $F_1(\sigma^*)$ and $F_2(\sigma^*)$. For $\sigma^* < \sigma_t$, cells grow logistically, whereas for $\sigma^* > \sigma_t$, cells die. These effects are local in space as the value of the shear stress depends on the position in the scaffold, and the overall profile of the flow.

where k_0 is the permeability of the cell-free scaffold.

We require an expression for the shear stress σ^* in Equation (2.6). We follow Whittaker et al. (2009) and Shakeel et al. (2013) and write,

$$\sigma^* = \frac{4\mu\tau}{R_0} \frac{\|\mathbf{u}_r^*\|}{\hat{\phi}(N^*)}, \quad (2.11)$$

as the shear stress experienced by cells at the pore scale in terms of the Darcy velocity, where R_0 is the typical radius of a pore and τ is the tortuosity of a typical fluid path.

Finally we specify the functions $F_1(\sigma^*)$ and $F_2(\sigma^*)$ to be

$$F_1(\sigma^*) = 1 - \left(\frac{1}{2}\right) (\tanh[g(\sigma^* - \sigma_t)] + 1), \text{ and } F_2(\sigma^*) = \left(\frac{1}{2}\right) (\tanh[g(\sigma^* - \sigma_t)] + 1), \quad (2.12)$$

where g and σ_t are sharpness and threshold parameters. Caricatures of these functions are plotted in Figure 2. These functions model smoothed step-function behaviour and are commonly used in the literature (Coletti et al., 2006; Shakeel et al., 2013). These functions capture logistic growth for small and moderate shear stress, and cell death at large values of shear stress.

We nondimensionalise as follows

$$\begin{aligned} (x^*, y^*) &= L(x, y), \quad \nabla^* = \frac{1}{L} \nabla, \quad (N^*, N_0^*) = N_c(N, N_0), \quad \hat{\phi}(N^*) = \phi_0 \phi(N), \\ k^*(N^*) &= k_0 \phi_0^3 k(N), \quad p^* = (p_0 - p_1)p + p_1, \quad \mathbf{u}^* = \frac{k_0 \phi_0^3 (p_0 - p_1)}{\mu L} \mathbf{u}, \quad \mathbf{u}_r^* = \frac{Q_c}{L} \mathbf{u}_r, \\ Q_0^* &= \frac{k_0 \phi_0^3 (p_0 - p_1)}{\mu} Q_0, \quad \sigma^* = \frac{4\mu\tau Q_c}{LR_0 \phi_0} \sigma, \quad t^* = \frac{t}{\beta}, \end{aligned} \quad (2.13)$$

leading to the following nondimensional system of equations,

$$\mathbf{u} = -k(N) \nabla p, \quad \nabla \cdot \mathbf{u} = 0, \quad (2.14a, b)$$

$$\frac{\partial N}{\partial t} = F_1(\sigma)N(1-N) - F_2(\sigma)N + \delta \nabla^2 N, \quad (2.14c)$$

$$Q_0 = \int_0^1 -k(N(0, \hat{y}, t)) \frac{\partial p}{\partial x}(0, \hat{y}) d\hat{y}, \quad \mathbf{u}_r = \frac{\mathbf{u}}{Q_0}, \quad (2.14d,e)$$

$$\phi(N) = (1 - \rho N), \quad k(N) = \phi(N)^3, \quad \sigma = \frac{\|\mathbf{u}_r\|}{\phi(N)}, \quad (2.14f,g,h)$$

$$F_1(\sigma) = 1 - \left(\frac{1}{2}\right) (\tanh[g_c(\sigma - \sigma_c)] + 1), \quad F_2(\sigma) = \left(\frac{1}{2}\right) (\tanh[g_c(\sigma - \sigma_c)] + 1), \quad (2.14i,j)$$

where $\rho = vN_c$ is the maximum available fraction of the pore space the cells can occupy, $\delta = D_n/\beta L^2$ is the ratio of proliferation and diffusion timescales, $g_c = (4\mu\tau Q_c)/(LR_0\phi_0)g$ is a sharpness parameter, and $\sigma_c = (LR_0\phi_0)/(4\mu\tau Q_c)\sigma_t$ is the threshold parameter.

The nondimensional boundary conditions are

$$\mathbf{u} \cdot \mathbf{n} = 0 \quad \text{at } y = 0, 1, \quad 0 \leq x \leq 1, \quad (2.15)$$

$$p = 1 \quad \text{at } x = 0, \quad 0 \leq y \leq 1, \quad \text{and} \quad p = 0 \quad \text{at } x = 1, \quad 0 \leq y \leq 1, \quad (2.16)$$

$$\mathbf{n} \cdot \nabla N = 0 \quad \text{for } \mathbf{x} \in \partial[0, 1]^2, \quad (2.17)$$

with the initial data

$$N(x, y, 0) = N_0(x, y). \quad (2.18)$$

Equations (2.14)-(2.18) are a modified form of those used by Shakeel et al. (2013), where we have neglected nutrient transport and nonlinear cell diffusion, but included a mechanism for cell death induced by high shear stress.

2.2 Lattice Model

We idealize the scaffold domain of length L as an n by n square lattice representing the connectivity between pores. At each node we specify the local cell density together with fluid pressures which we use to define volumetric flow rates along the edges between nodes. We assume these edges represent pipes of length $l = L/n$. See Figure 1 for a diagram of this idealization.

We prescribe a constitutive law relating the pressure p_i at each node i with the volumetric flow rate between the nodes, where $1 \leq i \leq n^2$. The particular form of this relationship depends on the microstructure of the scaffold under consideration, but for simplicity we assume Poiseuille flow between each node, so that

$$q_{ij}^* = \frac{\pi(R_{ij}^*)^4}{8l\mu} (p_i^* - p_j^*), \quad (2.19)$$

where q_{ij}^* is the volumetric flow rate (m^3s^{-1}) from node i to node j , and R_{ij}^* is the effective radius of the pipe between these nodes, which will depend on the cell density at the nearby nodes (see Equation (2.26)).

Due to incompressibility, we can write conservation of mass at each node as

$$\sum_{j=1}^{n^2} A_{ij} q_{ij}^* = \begin{cases} f_{li}, & 1 \leq i \leq n, \\ 0, & n < i \leq n^2 - n, \\ -f_{ir}, & n^2 - n < i \leq n^2, \end{cases} \quad (2.20)$$

where A_{ij} is the unweighted undirected adjacency matrix of the lattice representing the connectivity of nodes, and f_{li} and f_{ir} are the volumetric flow rates into the nodes at the left and the right side of the scaffold respectively, which will be used to prescribe the total volumetric flow rate into the scaffold. We have that $A_{ij} = 1$ if there is an edge between node i and node j , and otherwise $A_{ij} = 0$. While we only consider a square lattice here, this formulation is general and any pore network topology can be accounted for by providing a different adjacency structure.

As in Section 2.1 we prescribe a pressure drop across the domain. We fix the pressure upstream of the left boundary as p_0 , and the pressure downstream of the right boundary as p_1 . Then the volumetric flow rate of fluid entering each node at the left is given by $f_{li} = (\pi R_0^4 (p_0 - p_i^*)) / (8l\mu)$ for $1 \leq i \leq n$, and the volumetric flow rate of fluid leaving each node along the right by $f_{ir} = (\pi R_0^4 (p_i^* - p_1)) / (8l\mu)$ for $n^2 - n < i \leq n^2$, where R_0 is the radius of pipes entering and exiting the scaffold.

We combine equations (2.19) and (2.20) together with the expressions for the boundary volumetric flow rates f_{li} and f_{ir} , to find that for all nodes i ,

$$\sum_{j=1}^{n^2} A_{ij} (R_{ij}^*)^4 (p_i^* - p_j^*) = \begin{cases} R_0^4 (p_0 - p_i^*), & 1 \leq i \leq n, \\ 0, & n < i \leq n^2 - n, \\ -R_0^4 (p_i^* - p_1), & n^2 - n < i \leq n^2. \end{cases} \quad (2.21)$$

Equations (2.21) represent an algebraic system of n^2 equations for the nodal pressures, p_i^* . As before, the physically relevant boundary condition is a constant volumetric flow rate into the scaffold. We exploit the linearity of the fluid problem above to rescale the fluid variables to match this condition. The total volumetric flow rate into the pipes along the left boundary is

$$Q^* = \sum_{i=1}^n \frac{\pi R_0^4}{8l\mu} (p_0 - p_i^*). \quad (2.22)$$

We rescale the volumetric flow rates q_{ij}^* by,

$$q_{ij}^{r*} = q_{ij}^* \frac{Q_l}{Q^*}, \quad (2.23)$$

where Q_l is the volumetric flow rate into the scaffold. Note that Q_l has dimensions of $\text{m}^3 \text{s}^{-1}$, whereas for the 2-D spatially continuous model, the flow rate Q_c had dimensions of $\text{m}^2 \text{s}^{-1}$. If we assume that the mean fluid velocity (not the Darcy velocity) into the pore space of the scaffold along the left boundary is the same between the two models, we must have $Q_c / (L\phi_0) = Q_l / (n\pi R_0^2)$ where the factor of πR_0^2 is the cross-sectional area of each pipe, and n accounts for the number of pipes along the leftmost boundary. Hence $Q_l = (n\pi R_0^2 Q_c) / (L\phi_0)$, and we use this relationship in the remainder of the paper.

Again assuming that cells grow logistically, die, and diffuse to neighbouring nodes, the evolution equation for the cell density N_i^* at node i is

$$\frac{dN_i^*}{dt^*} = \beta \left(F_1^l(\sigma_i^*) N_i^* \left(1 - \frac{N_i^*}{N_c} \right) - F_2^l(\sigma_i^*) N_i^* \right) + D_l \sum_{j=1}^{n^2} A_{ij} (N_j^* - N_i^*), \quad i = 1 \dots n^2, \quad (2.24)$$

where D_l is the local cell diffusion rate to move between neighboring nodes, σ_i^* is a local average of the shear stress defined in Equation (2.29), and the functions F_1^l and F_2^l model the effect of shear stress on cell growth and death. Equations (2.24) are analogous to Equation (2.6). In particular, the cell

proliferation rate β and maximum cell density N_c have the same meaning as in Equation (2.6). The cell diffusion rate between nodes can be related to cell diffusion on the length scale of the scaffold D_n by $D_l = D_n/l^2 = n^2 D_n/L^2$. We specify an initial condition at each node as

$$N_i^*(0) = N_{i0}^*. \quad (2.25)$$

We model the effect of cell growth on the fluid flow by taking the effective radius of a pipe to depend on the nearby cell densities as

$$R_{ij}^* = R_0 \left(1 - \frac{\nu}{2} (N_i^* + N_j^*) \right), \quad (2.26)$$

where again ν represents cell volume. Equation (2.26) models pipes with radii that linearly decrease as the cell density increases at nearby nodes. Note that we must have $\nu N_c \leq 1$ for this radius to be non-negative for all feasible cell densities. This relationship is analogous to the porosity relationship given in Equation (2.9).

We compute the shear stress in each pipe under the assumption of Poiseuille flow made in Equation (2.19). The local velocity profile in the pipe R_{ij}^* is

$$u_{ij}^*(r^*) = -2 \left(\frac{(R_{ij}^*)^2 - (r^*)^2}{\pi (R_{ij}^*)^4} \right) q_{ij}^{r*}, \quad (2.27)$$

where $0 \leq r^* \leq R_{ij}^*$ is the radial coordinate. The magnitude of the shear stress at the wall of each pipe is then

$$\sigma_{ij}^* = \mu \left| \frac{\partial u_{ij}^*}{\partial r^*} (R_{ij}^*) \right| = \frac{4\mu}{\pi (R_{ij}^*)^3} |q_{ij}^{r*}|. \quad (2.28)$$

As cell densities are defined at the nodes, we must relate the shear stress in each idealized pipe to an average shear stress σ_i^* at each node. We note that adding the shear stresses from the four neighboring nodes accounts for the total volumetric flow rate twice, so we sum the shear stress in each pipe connected to node i and divide by 2 to obtain

$$\sigma_i^* = \frac{1}{2} \sum_{j=1}^{n^2} A_{ij} \sigma_{ij}^* = \sum_{j=1}^{n^2} A_{ij} \frac{2\mu}{\pi (R_{ij}^*)^3} |q_{ij}^{r*}|. \quad (2.29)$$

We model the influence of this averaged shear stress on cell proliferation and death as before by

$$F_1^l(\sigma_i^*) = 1 - \left(\frac{1}{2} \right) (\tanh[g(\sigma_i^* - \sigma_t)] + 1), \quad F_2^l(\sigma_i^*) = \left(\frac{1}{2} \right) (\tanh[g(\sigma_i^* - \sigma_t)] + 1). \quad (2.30)$$

These functions have the same form as those in Equations (2.12); see Figure 2 for a visualization.

For each $1 \leq i, j \leq n^2$ we nondimensionalize by taking

$$p_i^* = (p_0 - p_1)p_i + p_1, \quad Q^* = \frac{\pi R_0^4 (p_0 - p_1)}{8l\mu} Q, \quad (N_i^*, N_{i0}^*) = N_c (N_i, N_{i0}),$$

$$q_{ij}^{r*} = \frac{n\pi R_0^2 Q_c}{L\phi_0} q_{ij}^r, \quad q_{ij}^* = \frac{\pi R_0^4 (p_0 - p_1)}{8l\mu} q_{ij}, \quad \sigma_i^* = \frac{2\mu Q_c}{L\phi_0 R_0} \sigma_i, \quad t^* = \frac{t}{\beta}, \quad R_{ij}^* = R_0 R_{ij}, \quad (2.31)$$

from which we obtain

$$q_{ij} = R^4(N_i, N_j)(p_i - p_j), \quad (2.32a)$$

$$\sum_{j=1}^{n^2} A_{ij} q_{ij} = \begin{cases} 1 - p_i, & 1 \leq i \leq n, \\ 0, & n < i \leq n^2 - n, \\ -p_i, & n^2 - n < i \leq n^2, \end{cases} \quad (2.32b)$$

$$\frac{dN_i}{dt} = F_1^l(\sigma_i) N_i (1 - N_i) - F_2^l(\sigma_i) N_i + \delta n^2 \sum_{j=1}^{n^2} A_{ij} (N_j - N_i), \quad (2.32c)$$

$$Q = \sum_{i=1}^n 1 - p_i, \quad q_{ij}^r = q_{ij} \frac{1}{Q}, \quad R_{ij} = 1 - \frac{\rho}{2} (N_i + N_j), \quad \sigma_i = n \sum_{j=1}^{n^2} A_{ij} R_{ij} |q_{ij}^r|, \quad (2.32d,e,f,g)$$

$$F_1^l(\sigma_i) = 1 - \left(\frac{1}{2}\right) (\tanh[g_l(\sigma_i - \sigma_l)] + 1), \quad F_2^l(\sigma_i) = \left(\frac{1}{2}\right) (\tanh[g_l(\sigma_i - \sigma_l)] + 1), \quad (2.32h)$$

where $i = 1 \dots n^2$, $\delta = (D_n)/(L^2\beta)$ is the ratio of proliferation and diffusion timescales, $\rho = vN_c$ is the maximum available fraction of pore radius cells can occupy, $g_l = (2\mu Q_c g)/(LR_0\phi_0)$ is a sharpness parameter, and $\sigma_l = (LR_0\phi_0\sigma_t)/(2\mu Q_c)$ is the shear stress threshold parameter. Note that ρ and δ are common between the lattice and continuum models, but the parameters g_l and σ_l are not. We also have the initial data

$$N_i(0) = N_{i0}, \quad 1 \leq i \leq n^2. \quad (2.33)$$

In addition to fundamental differences between a spatial continuum and a discrete lattice, there are two significant constitutive differences between our models. The exponents in the relationships between the Darcy velocity, \mathbf{u}_r , or volumetric flow rates, q_{ij} , which play analogous roles, and the cell density are not the same between the two models. To see this, we write Equation (2.14a) using the permeability k and porosity ϕ in Equations (2.14f,g) as

$$\mathbf{u} = -(1 - \rho N)^3 \nabla p, \quad (2.34)$$

and similarly rewrite (2.32a) using the effective pipe radii from Equation (2.32f) to find,

$$q_{ij} = \left(1 - \frac{\rho}{2} (N_i + N_j)\right)^4 (p_i - p_j). \quad (2.35)$$

These relationships show that for a given local pressure drop, the local Darcy velocity in the PDE is larger in regions of high cell density than the corresponding volumetric flow rate in the lattice.

There are also differences in the nondimensional expressions for the shear stress in each model (see Equation (2.14h) and Equation (2.32g)). To visualize how these constitutive differences lead to quantitatively different predictions, consider a uniform cell density in both models. Let $N(x, y, t) = \hat{N}(t)$ for all (x, y) in the domain and $N_i(t) = \hat{N}(t)$ for $1 \leq i \leq n^2$. For a uniform cell density, the fluid flow is uniform so $\|\mathbf{u}_r\| = 1$ and $q_{ij}^r = 1/n$ for all i, j . This can be seen from solving Equations (2.14a,b) and (2.14d-h) for the PDE, or Equations (2.32a,b), and (2.32d-g) for the lattice. Note that in the lattice, we have nondimensionalized such that the total volumetric flow rate into the scaffold from the left boundary is 1, leading to the flow in each horizontal pipe being $1/n$ as there are n pipes along the boundary. We can then compute the (spatially uniform) shear stress for the PDE model as,

$$\sigma = \frac{\|\mathbf{u}_r\|}{\phi(N)} = \frac{1}{1 - \rho \hat{N}}, \quad (2.36)$$

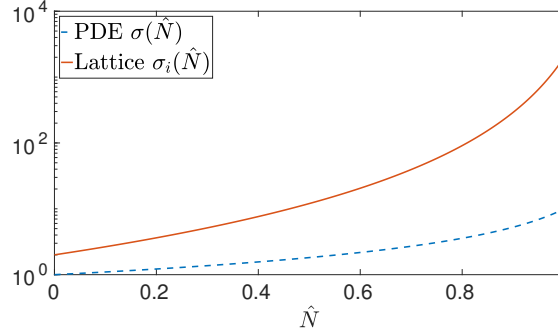


FIG. 3: Plots of the uniform shear stress for a uniform cell density distribution \hat{N} , for $\rho = 0.9$. Note that the vertical axis is scaled logarithmically.

and for the lattice model as,

$$\sigma_i = n \sum_{j=1}^{n^2} A_{ij} R_{ij} |q_{ij}^r| = \frac{2}{(1 - \rho \hat{N})^3}. \quad (2.37)$$

We plot these shear stresses as functions of \hat{N} in the interval $[0, 1]$ in Figure 3. For large cell densities, the shear stress experienced by the cells in the continuum and lattice models differs by two orders of magnitude. These differences between Equations (2.36) and (2.37) prevent quantitative agreement between our models; we emphasize qualitative differences between the model predictions by exploring ranges of parameters in the following discussion.

2.3 Model Parameters

The continuum and lattice models contain a number of parameters that can vary significantly between tissue engineering experiments. As we are primarily interested in informing model selection, rather than constructing quantitatively accurate models, we focus on the orders of magnitude over which these parameters vary. Table 1 lists the range of parameter values found in the literature. Using these values we estimate the ranges of the two nondimensional parameters that appear in both models, and estimate the number of pores per side of the square lattice n .

The shear stress threshold σ_l and the sharpness parameter g are not readily available in the literature. We treat the nondimensional thresholds σ_l and σ_c as model parameters and demonstrate model behaviours as they vary. Motivated by existing theoretical models in which the function F_1 approximated a step function (Shakeel et al., 2013), we set $g_l = g_c = 60$. In our simulations we fix $\rho = 0.9$ so that cell growth significantly affects the effective permeability of the scaffold.

2.4 Numerical Simulations

The lattice size n and diffusion to proliferation rate δ are varied to demonstrate the range of qualitative behaviours displayed by these models. Specifically we take $n = 25, 50, 75$, and 100 for the lattice simulations, and $\delta = 10^{-4}, 10^{-3}, 10^{-2}$, and 10^{-1} for both models. We take values of both lattice and PDE thresholds to be $\sigma_c = \sigma_l = 2.5, 5, 7.5, 10, 100$, and 1000.

Parameter	Expression	Value
Cell volume ^{*†}	v	$10^{-18} - 10^{-17} \text{m}^3/\text{cell}$
Maximum cell density [†]	N_c	$10^{17} - 10^{18} \text{cell}/\text{m}^3$
Scaffold length ^{*†¶}	L	$10^{-3} - 10^{-2} \text{m}$
Pore length scale ^{†¶}	l, R_0	$10^{-5} - 10^{-3} \text{m}$
Cell proliferation timescale ^{*†}	$1/\beta$	$10^4 - 10^6 \text{s}$
Viscosity [†]	μ	$10^{-4} - 10^{-3} \text{kg}/(\text{ms})$
Cell-free scaffold porosity ^{†§}	ϕ_0	40-97%
Pump flow rate ^{†¶}	Q_c	$10^{-5} - 10^{-3} \text{m}^2/\text{s}$
Cell diffusion rate ^{*†}	D_n	$10^{-12} - 10^{-11} \text{m}^2/\text{s}$
Ratio of timescales	$\delta = D_n/L^2\beta$	$10^{-4} - 10^1$
Maximum cell volume fraction	$\rho = vN_c$	$10^{-2} - 1$
Pores per lattice side	$n = L/l$	$1 - 10^3$

Table 1: Parameters used in the models. ^{*} Vafai (2010), [†] Shakeel et al. (2013), [‡] McCoy et al. (2012), [§] Truscillo et al. (2012), [¶] Glowacki et al. (1998).

The continuum model given by Equations (2.14)-(2.18) was simulated using the finite element solver Comsol with 24,912 triangular elements. Time and space refinements were carried out to ensure that the numerical approach converged. Additionally, the results found via Comsol were consistent with those found from a finite-difference scheme implemented to solve the same model. The lattice model given by Equations (2.32)-(2.33) was solved using an explicit adaptive Runge-Kutta method in Matlab. To ensure accuracy of our simulations with respect to the bifurcation behaviour discussed in Section 3.3, we constrain the maximum Runge-Kutta time step to be 10^{-3} (Christodoulou, 2008). Specific simulations were also undertaken with a fixed time step Runge-Kutta scheme with refinements in the size of the time step to ensure convergence.

We consider our initial condition to be a perturbed uniform cell density to demonstrate the emergence of spatial structure due to non-uniform growth. On a lattice with $n = 100$ nodes per side, we set $N_i(0) = 0.1 + 10^{-4}\xi_i$ where $\xi_i \sim \mathcal{N}(0, 1)$ is a normally distributed noise term. One realization of this perturbed uniform state is then interpolated on the smaller lattices, or onto the triangular elements of the continuum model, so that all simulations have approximately consistent initial conditions. We compute mean cell densities as,

$$\hat{N}(t) = \left(\frac{\sum_{i=1}^{n^2} N_i(t)}{n^2} \right), \quad (2.38)$$

for the lattice and

$$\hat{N}(t) = \int_0^1 \int_0^1 N(x, y, t) dx dy, \quad (2.39)$$

for the PDE (computed numerically using the triangular elements from the finite element scheme).

3. Results and Discussion

In Section 3.1 we discuss how the perturbed uniform initial data undergoes a change from uniform logistic growth to death in local regions of the scaffold, leading to spatial heterogeneity in cell density which is observed over long timescales. In Section 3.2 we discuss the onset time of this spatial patterning. In

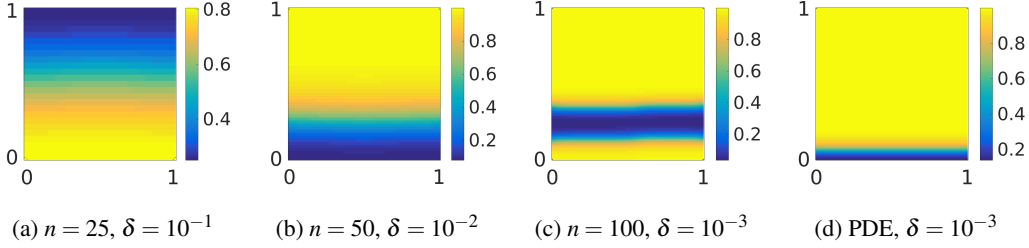


FIG. 4: Plots of the cell density with $t = 30$ and $\sigma_c = \sigma_l = 10$ demonstrating simple spatial patterning at various values of diffusion, $\delta \geq 10^{-3}$.

Section 3.3 we discuss oscillations in cell density that are observed only in simulations of the lattice model. Finally, in Section 3.4, we compare the model predictions for the final cell densities.

3.1 Spatial Heterogeneity

Over long timescales (nondimensional times of $t > 10$) all of our simulations exhibit significant spatial heterogeneity in cell density and shear stress. In some regions of the scaffold the cell density is close to the nondimensional carrying capacity, and there is reduced fluid flow and low shear stress in these areas. There are also regions of high fluid flow and associated shear, and low cell density. The spatial structure of the cell density distributions depends heavily on the parameter δ .

For large values of the parameter ($\delta \geq 10^{-3}$), a single region or channel develops with low cell density, and through which the majority of fluid passes. In the remainder of the domain, there is little fluid flow and the cell density is high; see Figure 4. The location of the large fluid channel, corresponding to regions of low cell density, depends on the initial data and parameter values, but we always observe a single channel for $\delta \geq 10^{-3}$. For brevity we plot only the cell density distributions in the scaffold, as the associated shear stress can be inferred from these plots (the fluid flow is always low in regions of high cell density and vice versa).

For $\delta = 10^{-4}$, we find significantly more spatial structure in the final cell density distributions. Figure 5 shows plots of the cell density at various times for lattice sizes $n = 25, 50$ and 100 , with threshold parameter $\sigma_l = 2.5$. After a period of growth, the initial uniform state rapidly breaks up into several aggregates of high cell density surrounded by regions of low cell density, which then evolve slowly due to diffusion and shear stress mediated cell growth and death. For the smallest lattice size ($n = 25$), this process stabilizes quickly leading to a steady state cell density within the first $t = 10$ time units (compare the cell density distributions for $n = 25$ and $t = 10, 15$, and 30 in Figure 5). For $n = 100$, many interior clusters slowly shrink as the cell aggregates along the top and bottom boundaries of the scaffold continue to grow over a longer timescale. Figure 6 shows cell density distribution plots for $\sigma_l = 7.5$. Note that for each n and t , the total area of high cell density is larger in Figure 6 than in 5. For both $\sigma_l = 2.5$ and $\sigma_l = 7.5$, the number of clusters of high cell density is initially greater in the $n = 100$ case after the onset of non-uniform growth, but there is a coarsening over time which reduces the number of distinct fluid channels and disconnected regions of high cell density. In comparison, the number of disconnected regions of high cell density is larger in the smaller lattices by the end of the simulation time in both Figures 5 and 6 (compare the $t = 30$ plots for $n = 25$ and $n = 100$ in both Figures).

Note that in Figure 5 the coarsening for the $n = 100$ lattice involves small clusters of high cell density disappearing, while for Figure 6 it is primarily channels of low cell density that disappear over

time. This difference in long-time behaviour can be understood via the threshold parameter σ_l . When $\sigma_l = 2.5$, cells die at relatively low values of shear stress and the overall cell density is low so cells recede away from regions of high fluid flow. For $\sigma_l = 7.5$ cells can withstand much more shear and grow over a much larger proportion of the scaffold, filling in small channels of fluid flow over time.

These results demonstrate a diverse range of behaviour for the lattice models. Figure 7 illustrates predictions from the PDE model for the cell density distribution over the spatial domain at various times and for four values of the threshold parameter σ_c . This model also exhibits transient dynamics where clusters of high cell density form, and then coarsen into larger regions of high cell density as in the $n = 100$ lattice shown in Figures 5 and 6. Overall there are more regions of high cell density in the PDE model compared to the lattice simulations, which is consistent with the shear stress predictions given in Figure 3 (for the same cell density, this plot shows lower predicted shear stress values for the PDE model compared to the lattice model).

In Figure 8, we plot time series of mean cell densities, $\hat{N}(t)$, for lattice simulations with $n = 25, 50$, and 100, as well as for the PDE. The $n = 25$ lattice quickly reaches a spatial equilibrium for each σ_l , whereas the larger $n = 100$ simulations show growth and death processes over a longer timescale, and in some cases these have not reached an equilibrium value at the end of the simulations at $t = 30$ (compare the long time behaviour in Figures 8a and 8c). We truncate the numerical experiments here partly because variations in cell density beyond this point for all simulations were small, and partly because this period of time would exceed most *in vitro* tissue engineering experiments as $t = 30$ would typically be on the order of months. All simulations shown in Figure 8 grow logistically at the same rate until some region of the scaffold reaches the shear stress threshold σ_l or σ_c leading to non-uniform growth, and eventually to differences in final mean cell densities.

We observe less spatial structure in the PDE simulations than in the lattice simulations (compare Figures 5 and 6 with Figure 7). We quantify spatial variation in cell density with a heterogeneity function. For simplicity we choose

$$E(N_1, \dots, N_{n^2}) = \frac{1}{n} \sum_{j=1}^{n^2} \sum_{i=1}^{n^2} A_{ij} |N_i - N_j|, \quad (3.1)$$

which is the total absolute difference in cell density between adjacent nodes throughout the lattice. The function satisfies $E \geq 0$ with $E = 0$ only for a homogeneous cell density distribution. The PDE solutions were interpolated onto a square grid with a size of 100 by 100, so the function defined by (3.1) can be seen as a discretization of the functional $\int_0^1 \int_0^1 |\partial_x N(x, y)| + |\partial_y N(x, y)| dx dy$ which is a measure of anisotropic total variation (van Gennip and Bertozzi, 2012).

In Figure 9 we plot values of this function for the simulated cell densities at $t = 30$. For the majority of parameter combinations simulated, the value of the heterogeneity given by (3.1) was lower for the PDE simulations than for any of the lattice simulations with the same parameters. Larger values of diffusion show significantly smaller values of spatial heterogeneity, and for most combinations of the parameters the larger lattice of size $n = 100$ has a lower value of E than the other two lattice sizes. Figure 10 shows a time series of this function for one choice of parameters for the lattice simulations and for a corresponding PDE simulation. For $n = 25, 50$, and for the PDE, the difference between the final heterogeneity and its maximal value is small, while for $n = 100$ the maximum value of E occurs around $t \approx 4$, and then slowly falls over time to a value that is significantly smaller. This allows for quantification of the coarsening behaviour described earlier that was qualitatively observed in Figure 6 for $n = 100$ and $t \geq 5$.

There is less spatial heterogeneity in the final cell densities of the PDE simulations than in the corresponding lattice model for all values of n and all values of σ_l and σ_c except for $\sigma_l = \sigma_c = 2.5$,

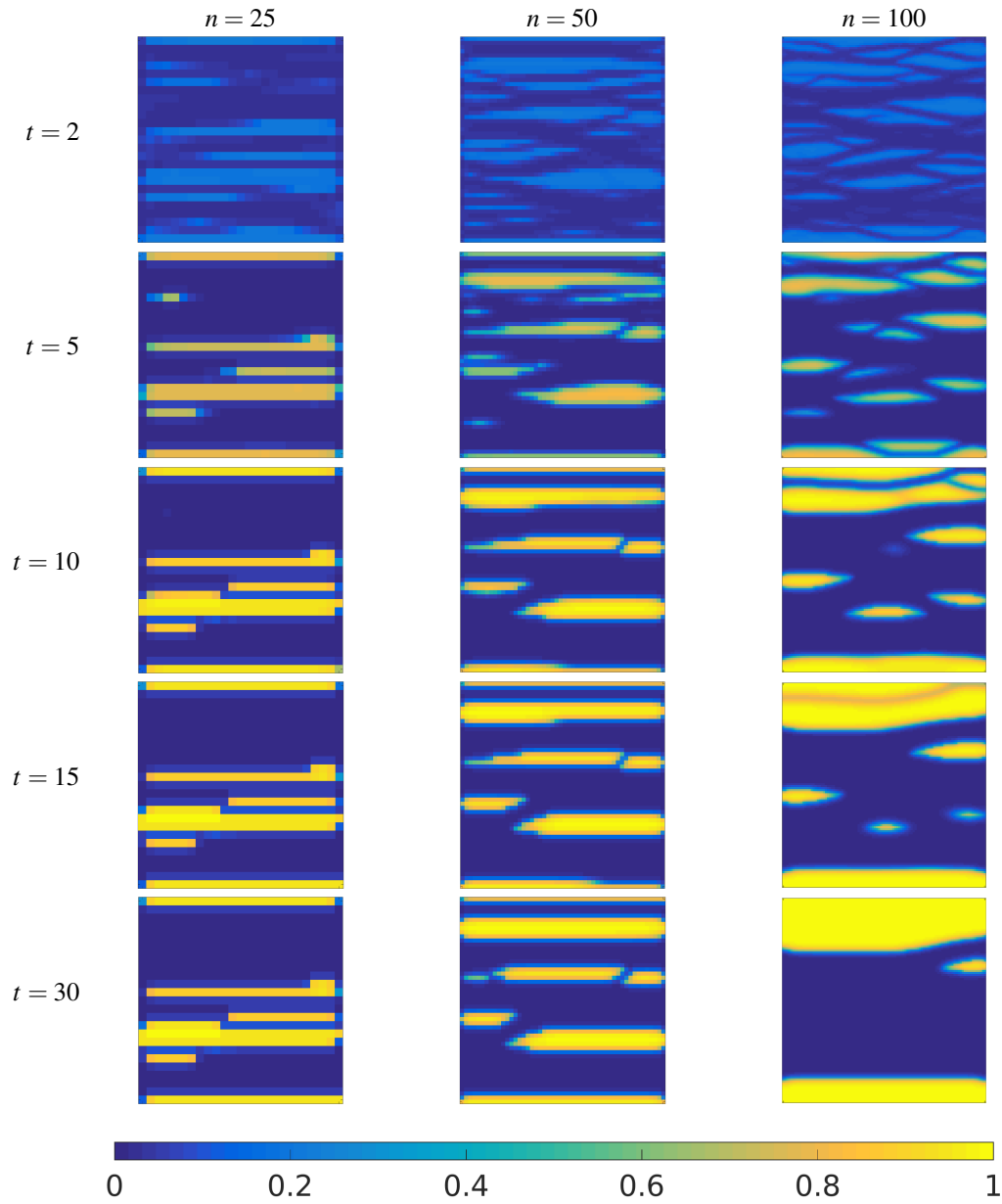


FIG. 5: Cell density plots with $\delta = 10^{-4}$, $\sigma_l = 2.5$ for three lattice sizes at different points in time.

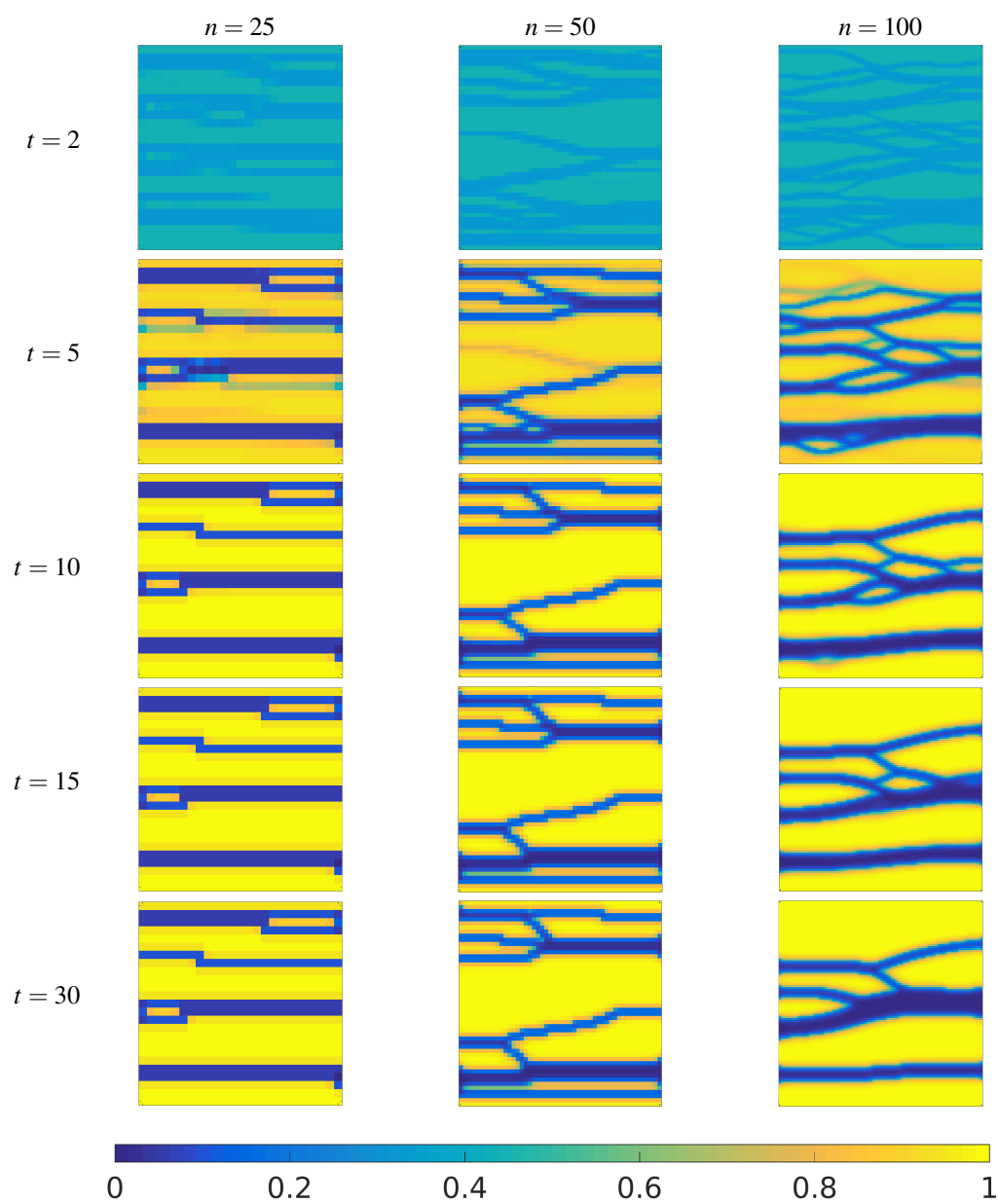


FIG. 6: Cell density plots with $\delta = 10^{-4}$, $\sigma_l = 7.5$ for three lattice sizes at different points in time.

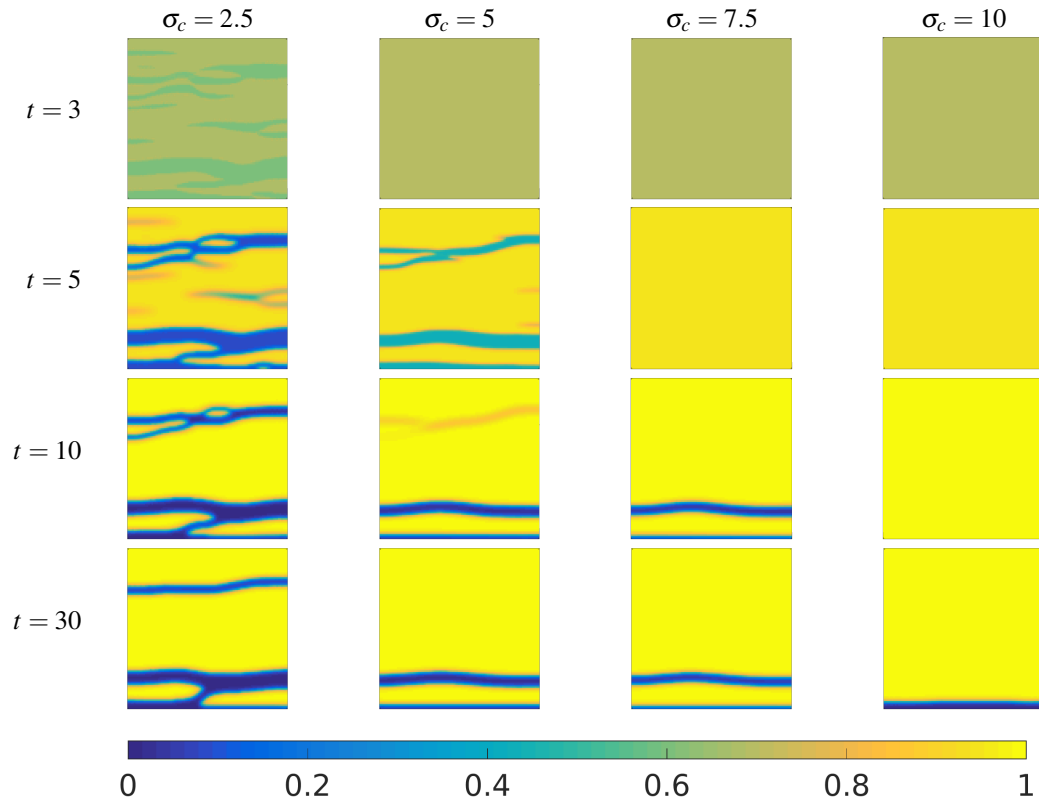


FIG. 7: Cell density plots with $\delta = 10^{-4}$, organized with $\sigma_c = 2.5, 5, 7.5$, and 10 from left to right, and at times $t = 2, 5, 10, 15$, and 30 from top to bottom.

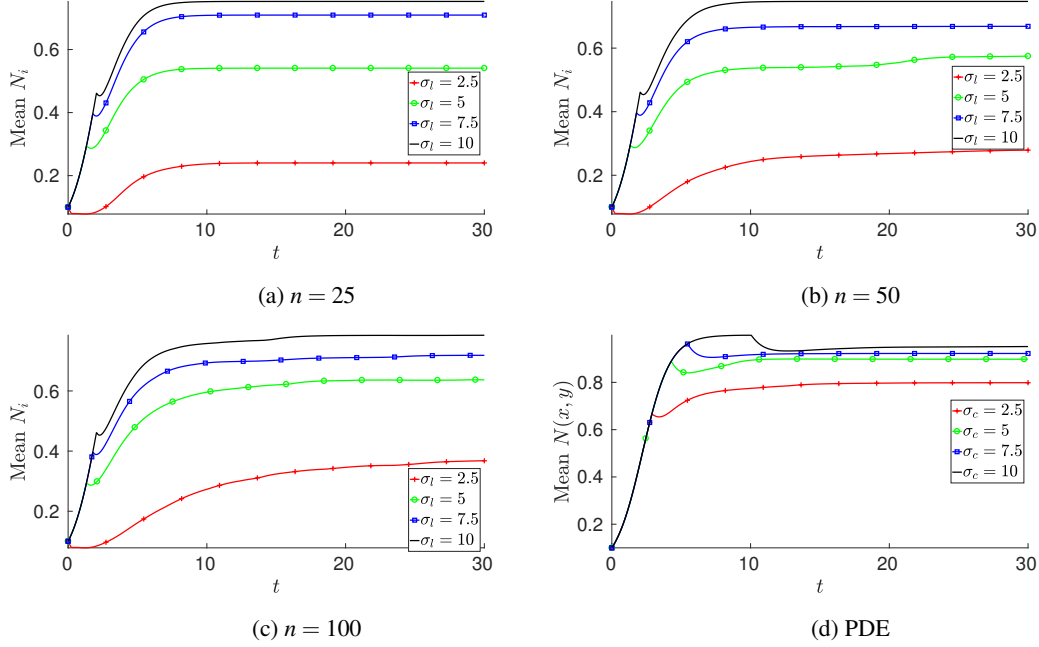


FIG. 8: Mean cell density plots over time for $\delta = 10^{-4}$ for lattice and PDE simulations.

where we note that for the cell density distributions in Figure 5 the cells have aggregated to the sides for $n = 100$ and $t = 30$ and hence created a single large channel in the center of the scaffold. We note that in Figure 10, there is a specific time at which spatial heterogeneity emerges (e.g. E is no longer 0), which corresponds to the onset of cell death in some regions of the scaffold.

3.2 Onset of Non-Uniform Patterning Due to Shear-Induced Cell Death

As the initial data are approximately uniform, the evolution of the cell density can be determined analytically up to the time that cell death occurs. For $\sigma \lesssim \sigma_c$, the cell growth is purely logistic. This bound is sharp in the limit of $g \rightarrow \infty$ where F_1 and F_2 become step-functions, but it is approximately obeyed for $g = 60$ so that for shear stress values below σ_c , cells will grow logistically. Hence, for a constant initial condition $N_0 \in [0, 1]$, we have

$$N(\mathbf{x}, t) = N_0 \frac{\exp(t)}{1 + N_0(\exp(t) - 1)}, \quad \mathbf{x} \in [0, 1]^2, \quad t < t_s, \quad (3.2)$$

where t_s is the time that it takes for the shear stress to become approximately equal to the threshold parameter, and hence for the cells to no longer undergo uniform logistic growth everywhere.

From Equation (2.36) we see that t_s may be defined implicitly by

$$\sigma_c \approx \sigma(t_s) = \frac{1}{1 - \rho N(t_s)}. \quad (3.3)$$

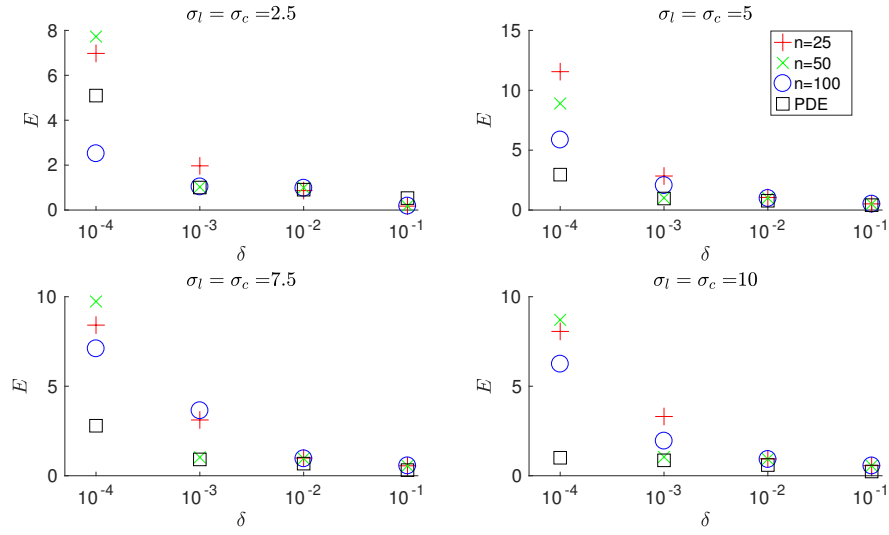


FIG. 9: Plots of the heterogeneity of cell density defined by (3.1) over the four values of δ for several parameter combinations for the PDE and lattice models at $t = 30$. Note the variation in the ranges of the heterogeneity function E .

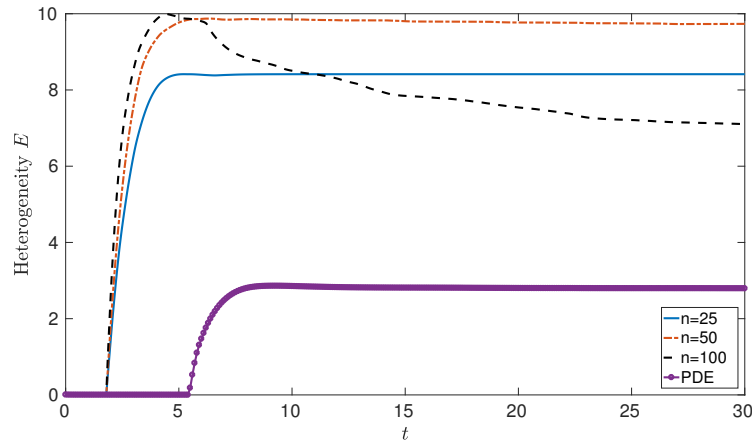


FIG. 10: Plots of the heterogeneity of cell density defined by (3.1) over the simulation time for $\delta = 10^{-4}$ and $\sigma_l = \sigma_c = 7.5$.

Substituting (3.2) into (3.3) gives

$$t_s = \ln \left(\frac{(\sigma_c - 1)(1 - N_0)}{N_0(1 - \sigma_c(1 - \rho))} \right). \quad (3.4)$$

Analogously for the lattice model, for $\sigma_i \lesssim \sigma_l$, the cell growth is purely logistic at each node. So for a constant initial condition $N_{i0} = N_0 \in [0, 1]$ for each i , we have

$$N_i(t) = N_0 \frac{\exp(t)}{1 + N_0(\exp(t) - 1)}, \quad 1 \leq i \leq n^2, \quad t < t_s, \quad (3.5)$$

t_s again being the time for the shear stress at some node to become comparable to the shear threshold. From Equation (2.37) we approximate t_s by

$$\sigma_l \approx \sigma_i(t_s) = \frac{2}{(1 - \rho N_i(t_s))^3}. \quad (3.6)$$

We substitute (3.5) into (3.6) to find

$$t_s = \ln \left(\frac{\left(2^{\frac{2}{3}} \sigma_l^{\frac{1}{3}} - 2 \right) (1 - N_0)}{N_0 \left(2 - 2^{\frac{2}{3}} \sigma_l^{\frac{1}{3}} (1 - \rho) \right)} \right). \quad (3.7)$$

We compare Equations (3.4) and (3.7) to the numerically computed values of t_s which correspond to $t_s \equiv \min_t (\max_x (\sigma(x, t)) > \sigma_c)$ for the PDE simulations, and $t_s = \min_t (\max_i (\sigma_i(t)) > \sigma_l)$ for the lattice simulations. In Figure 11 we plot values of t_s for all lattice and PDE simulations with varying δ , σ_c , and σ_l . We see excellent agreement between the analytical and numerical predictions for both the lattice and the PDE. We see that t_s does not depend on the lattice size n or the parameter δ except for the PDE simulation at $\sigma_c = 10$. We note that $\sigma_c = 10$ is a limiting case as Equation (3.4) indicates that $t_s \rightarrow \infty$ as $\sigma_c \rightarrow 10$ if the initial cell density distribution was exactly uniform.

The time t_s can be seen in Figure 8 where the form of the time series changes from a logistic curve, and for all values of σ_l and σ_c the mean cell density begins decreasing at this time. In most cases this period of decreasing mean cell density is short relative to the simulation timescale. The time t_s can also be seen in Figure 10 as the point where the heterogeneity increases sharply from $E = 0$, due to the onset of non-uniform growth.

3.3 Lattice Oscillations

A particularly interesting behaviour we observe in some lattice simulations are oscillations in cell density. Such oscillations are not found the PDE model. Figure 12 shows a time series plot of the cell density at every lattice node for $n = 10$ and $n = 25$. After a period of transient behaviour, the nodal cell densities oscillate in phase. Nodes that are growing ($\sigma_i < \sigma_l$) are coloured green with solid lines, and nodes that are dying ($\sigma_i > \sigma_l$) are coloured red with dashed lines. The mean cell density is plotted in blue, which is also oscillating but with a small amplitude. Thus the overall effect of the lattice oscillations on the mean cell density is small.

In regions of the scaffold where the local shear stress exceeds the threshold σ_l , cells are (exponentially) dying due to high shear stress. These nodes all have relatively low cell density and hence more

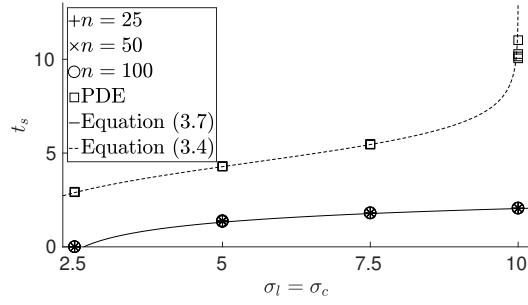


FIG. 11: Plots of the numerical values of t_s for all parameter combinations of $\delta = 10^{-1}, 10^{-2}, 10^{-3}, 10^{-4}$ and $\sigma_c = \sigma_l = 2.5, 5, 7.5$, and 10 for the PDE and lattice models. The symbols $+$, \times , the circle and the square are for the numerical solutions for lattice sizes $n = 25, 50, 100$ and the PDE respectively. The continuous lines are plots of the analytical approximations from (3.4) and (3.7).

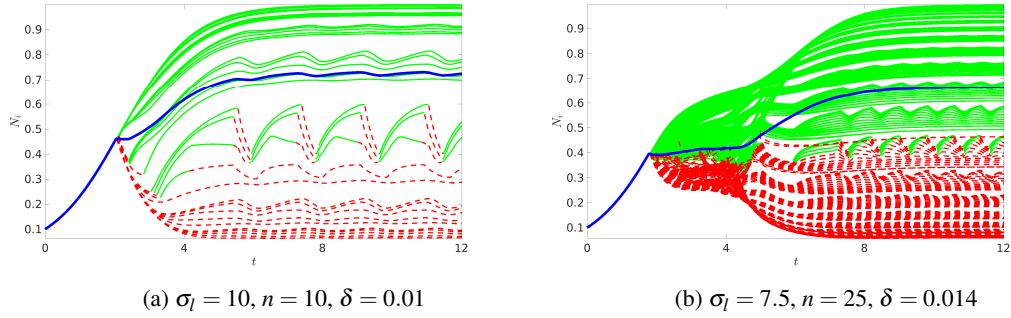


FIG. 12: Plots of the cell density of every node for different parameter combinations. Green solid lines correspond to the cells at that node growing logistically ($\sigma_i < \sigma_l$), and red dashed lines correspond to exponential death ($\sigma_i > \sigma_l$). The blue line shows the mean cell density.

fluid passes through them, maintaining this high value of shear stress. In other regions of the scaffold with low shear stress, cells grow logistically. Diffusion acts to move cells from regions of high density to low density, and so cells move from regions with low shear stress to regions of high shear stress. In certain parameter regimes, this process finds an equilibrium value where these regions separate, as in Figures 5 and 6, where between regions of growth and death there are some nodes of intermediate cell density. However, for certain values of n , σ_l , and δ , the movement and growth of cells gives rise to a different behaviour from this equilibrium as the growth of cells in regions of high cell density substantially affects fluid flow and shear stress throughout the entire scaffold. As seen in Figure 12, diffusion from growing regions can cause regions that are dying to increase in total cell density, and similarly, regions that are growing logistically can decrease in cell density due to diffusion.

We plot bifurcation diagrams of the maximal nodal oscillation amplitudes in Figures 13a-13b for several lattice sizes and two values of the threshold parameter, over a range of the parameter δ . After enough time has passed to ensure we are no longer observing transient dynamics, we compute the maximum nodal amplitude as $N_{osc} = \max_i \{ \max_t \{ N_i(t) \} - \min_t \{ N_i(t) \} \}$ to capture the largest oscillation. We plot the frequency ω_N of these nodal oscillations computed with the Fast Fourier Transform in Figures 13c-13d. We note that the frequency is the same for every node in the lattice.

These bifurcation diagrams show that for each n and σ_l , the one-dimensional parameter space over δ is composed of disconnected regions where oscillations are permitted (see behaviour illustrated in Figure 12), and regions where cell densities tend to steady states (see Figure 8). Further simulations within each of these regions (using different realizations of the perturbations of the initial data, for instance) have consistent behaviour, and we conjecture that these behaviours are generic within each region in parameter space demarcated by the bifurcation between steady state behaviour and oscillations. The number of disconnected regions in δ -space with oscillatory behaviour increases as n increases, and the maximal amplitudes decrease with increasing n . There is a trend of increasing oscillation frequency and decreasing nodal amplitude for larger values of δ for a given lattice size. The larger lattices have significantly smaller variations in mean cell density of the scaffold due to these oscillations. This is due to only a small subset of the nodes switching between growth and death behaviours during an oscillation. These oscillations do not occur in any of our PDE simulations. For large n , our simulations show that the amplitudes of oscillation in mean cell density decreases, as shown by the blue lines in Figure 12, and that the proportion of nodes switching between growth and death behaviours also decreases. In the other direction, for lattices of size $n = 5$ and smaller, no oscillations were observed. We refer to (Krause et al., 2017) for a discussion of Hopf bifurcations in a similar lattice system, where cells die due to high fluid pressure rather than shear stress. There we argue that the oscillations are due to a combination of nonlocal effects due to the quasi-static fluid problem, coupled with symmetry-breaking bifurcations in the lattice models.

3.4 Mean Cell Density Predictions

We can broadly understand the global behaviour of the numerical simulations by comparing their final mean cell densities computed via Equations (2.38) and (2.39). Figure 14 is a plot of the spatial mean of the cell density after 30 nondimensional units of time. For any given shear stress threshold and δ , the PDE model has a higher mean cell density. This is expected due to the differences between the constitutive assumptions for shear stress in each model (see Figure 3).

The value of the parameter δ has a non-monotonic effect for some lattice simulations. In particular, for $\sigma_c, \sigma_l \leq 10$, the maximum mean cell density for the $n = 50$ lattice occurs for the intermediate value

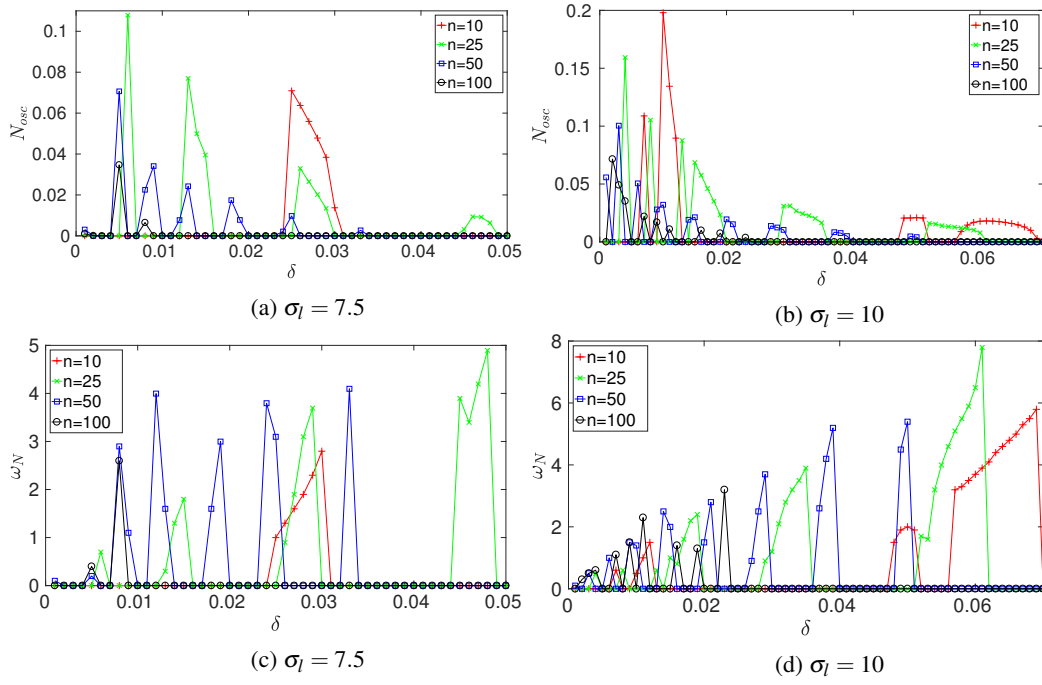


FIG. 13: Plots (a)-(b) are bifurcation diagrams showing the maximum magnitude of nodal oscillation in the lattice for different lattice sizes. This is plotted in steps of 0.001. Plots (c)-(d) are corresponding frequencies for these nodal oscillations.

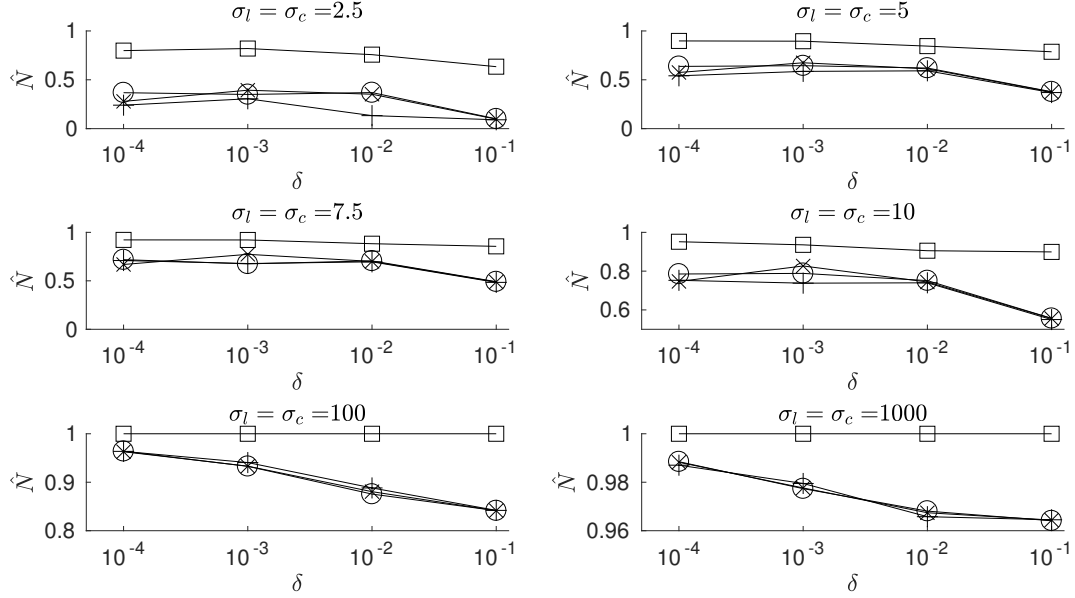


FIG. 14: Plots of the mean cell density \hat{N} at the final time $t = 30$ over the four values of δ for all parameter combinations for the PDE and lattice models. The symbols $+$, \times , \circ and \square are for the lattice sizes $n = 25, 50, 100$ and the PDE respectively. Note the variation in the ranges of the mean cell density \hat{N} .

of the diffusion parameter $\delta = 10^{-3}$. For the large value of $\delta = 10^{-1}$ in each plot, the lattice size is insignificant in determining the mean cell density. Similarly, for the large shear stress thresholds $\sigma_l = 100$, and 1000 shown in the bottom two plots, cell death occurs only in a very small region of the domain, so the lattice size is almost inconsequential in determining the final mean cell density. For $\sigma_l \leq 10$ and $\delta \leq 10^{-2}$, however, there are differences between the final mean cell density for different lattice sizes. This suggests that for applications where the ratio of proliferation to diffusion timescales is small, and where cells are very sensitive to high shear stress, the topology of the underlying pore network plays a role in determining the final mean cell density.

4. Conclusions

In this paper we have explored complementary lattice and continuum models for a bioactive porous tissue scaffold, and demonstrated several important differences in model behaviours. The lattice simulations show that considering finite pore networks when modelling cell growth within a porous scaffold will lead to qualitative differences compared with PDE models. Varying degrees of spatial heterogeneity in the cell density distribution are displayed in the lattice model, whereas for most of the parameter space the PDE solutions exhibit simpler spatial structures, such as one or two horizontal channels. The significant variation between different lattice sizes indicates that considering the spatial network explicitly has a nontrivial impact on pattern formation. The smoothing behaviour observed in both the PDE and large n lattice models is reminiscent of models of coarsening in condensed matter physics, where

initial spatial irregularities evolve into larger spatial structures. That this coarsening occurs at different timescales and to different degrees due to the size of the lattice is an unexpected result. We conjecture that, modulo constitutive differences, a PDE and a very large lattice (e.g. $n > 100$) should have comparable behaviour, but for smaller pore networks the finite structure of the lattice becomes important to the overall growth process within the scaffold.

We observe small amplitude oscillations in cell density exclusively in the lattice model. While the effects of these oscillations on the total mean cell density of the scaffold are small, their presence is an interesting effect of finite lattice size. Some tissue scaffolds are cyclically loaded to affect cell growth via mechano-transduction. In certain parameter regimes, this oscillatory forcing could interact in non-trivial ways with these shear-stress induced oscillations (Neler et al., 2016). We leave the investigation of such possibilities to future work.

While we observed quantitative differences between these paradigms (see Figure 14), we attribute some of these differences to the constitutive assumptions as shown in Equations (2.34)-(2.37), and these can vary between particular applications of these models. We have explored simulations using different functional forms of ϕ , k , and R_{ij} , as well as different values of ρ . These preliminary simulations were consistent with the qualitative differences reported here between lattice and continuum models. The constitutive choices we have made in this paper do give results that are consistent with Nava et al. (2013) in that our 2-D fluid model in the PDE over-predicts cell density compared with the 3-D fluid ('tube') model of the lattice.

These differences in the type of behaviours displayed by continuum and lattice models exist even though the network geometry studied here, a square grid lattice, is simple. In addition to a more complex network geometry, there are many components that could be included in this lattice model, such as a model of nutrient transport, or a more detailed microscale relationship between cell density and fluid flow. Nevertheless, these simple models give insight into the kinds of differences one can expect from each modelling paradigm.

For experiments involving small pore sizes or large constructs, the pore network is relatively dense and we expect continuum and lattice models to be comparable in terms of predicting cell proliferation and global fluid properties, such as scaffold permeability. For small scaffolds or scaffolds with large pores, however, we expect lattice models to significantly differ from continuum models in their predictions. The variations between the lattices of different size implies that a good model of the finite network geometry of a scaffold is important in understanding the tissue growth process for such scaffolds. Given a realistic description of the evolution of cells and fluid flow at the pore scale, our approach gives an alternative to continuum approaches such as mathematical homogenization in upscaling these microscale processes. Numerical solution of the lattice model is no more difficult than an equivalent discretization of a continuum model, and so the only practical disadvantage of using a lattice model would be the requirement of specifying the network topology, and determining appropriate fluid and cell properties at the scale of nodes in the network. We believe that pursuing these kinds of models can lead to novel insights in understanding the growth of artificial tissue, and eventually in developing clinically successful technologies.

5. Acknowledgements

D. Beliaev was partially funded by Engineering & Physical Sciences Research Council (EPSRC) Fellowship ref. EP/M002896/1.

References

- Barbotteau, Y., Irigaray, J. L., and Mathiot, J. F. (2003). Modelling by percolation theory of the behaviour of natural coral used as bone substitute. *Physics in Medicine and Biology*, 48(21):3611–3623.
- Bear, J. (1972). *Dynamics of Fluids in Porous Media*. American Elsevier, New York.
- Beard, T., Kaserman, D., and Osterkamp, R. (2013). *The Global Organ Shortage: Economic Causes, Human Consequences, Policy Responses*. Stanford University Press, Stanford.
- Chapman, L. A. C., Shipley, R. J., Whiteley, J. P., Ellis, M. J., Byrne, H. M., and Waters, S. L. (2014). Optimising Cell Aggregate Expansion in a Perfused Hollow Fibre Bioreactor via Mathematical Modelling. *PLoS ONE*, 9(8):e105813.
- Christodoulou, N. S. (2008). Discrete Hopf bifurcation for Runge-Kutta methods. *Applied Mathematics and Computation*, 206(1):346–356.
- Cimetta, E., Flaibani, M., Mella, M., Serena, E., Boldrin, L., De Coppi, P., and Elvassore, N. (2007). Enhancement of viability of muscle precursor cells on 3d scaffold in a perfusion bioreactor. *The International Journal of Artificial Organs*, 30(5):415–428.
- Coletti, F., Macchietto, S., and Elvassore, N. (2006). Mathematical Modeling of Three-Dimensional Cell Cultures in Perfusion Bioreactors. *Industrial & Engineering Chemistry Research*, 45(24):8158–8169.
- Cox, S. C., Thornby, J. A., Gibbons, G. J., Williams, M. A., and Mallick, K. K. (2015). 3d printing of porous hydroxyapatite scaffolds intended for use in bone tissue engineering applications. *Materials Science and Engineering: C*, 47:237–247.
- Geris, L., editor (2013). *Computational Modeling in Tissue Engineering*, volume 10 of *Studies in Mechanobiology, Tissue Engineering and Biomaterials*. Springer Berlin Heidelberg, Berlin, Heidelberg.
- German, C. L. and Madhally, S. V. (2016). Applications of Computational Modelling and Simulation of Porous Medium in Tissue Engineering. *Computation*, 4(1):7.
- Glowacki, J., Mizuno, S., and Greenberger, J. (1998). Perfusion Enhances Functions of Bone Marrow Stromal Cells in Three-Dimensional Culture - Biochemical and ultrastructural analyses. *Cell Transplantation*, 7(3):319–326.
- Hossain, M. S., Bergstrom, D. J., and Chen, X. B. (2015). Computational modelling of the scaffold-free chondrocyte regeneration: a two-way coupling between the cell growth and local fluid flow and nutrient concentration. *Biomechanics and Modeling in Mechanobiology*, 14(6):1217–1225.
- Iskratsch, T., Wolfenson, H., and Sheetz, M. P. (2014). Appreciating force and shape the rise of mechanotransduction in cell biology. *Nature Reviews Molecular Cell Biology*, 15(12):825–833.
- Kim, S. S., Penkala, R., and Abrahimi, P. (2007). A perfusion bioreactor for intestinal tissue engineering. *The Journal of Surgical Research*, 142(2):327–331.
- Krause, A. L., Beliaev, D., Van Gorder, R. A., and Waters, S. L. (2017). Analysis of Lattice and Continuum Models of Bioactive Porous Media. *arXiv:1702.08345 [q-bio]*.

- Lemon, G., Howard, D., Tomlinson, M. J., Buttery, L. D., Rose, F. R. A. J., Waters, S. L., and King, J. R. (2009). Mathematical modelling of tissue-engineered angiogenesis. *Mathematical Biosciences*, 221(2):101–120.
- Loh, Q. L. and Choong, C. (2013). Three-Dimensional Scaffolds for Tissue Engineering Applications: Role of Porosity and Pore Size. *Tissue Engineering Part B: Reviews*, 19(6):485–502.
- McCoy, R., Jungreuthmayer, C., and O’Brien, F. (2012). Influence of flow rate and scaffold pore size on cell behavior during mechanical stimulation in a flow perfusion bioreactor. *Biotechnology and Bioengineering*, 109(6):1583–1594.
- McDougall, S. (2002). Mathematical Modelling of Flow Through Vascular Networks: Implications for Tumour-induced Angiogenesis and Chemotherapy Strategies. *Bulletin of Mathematical Biology*, 64(4):673–702.
- Mely, H. and Mathiot, J.-F. (2012). Double site-bond percolation model for biomaterial implants. *Applied Physics A*, 106(3):635–644.
- Nava, M. M., Raimondi, M. T., and Pietrabissa, R. (2013). A multiphysics 3d model of tissue growth under interstitial perfusion in a tissue-engineering bioreactor. *Biomechanics and Modeling in Mechanobiology*, 12(6):1169–1179.
- Neler, K. H. L., Henstock, J. R., El Haj, A. J., Waters, S. L., Whiteley, J. P., and Osborne, J. M. (2016). The influence of hydrostatic pressure on tissue engineered bone development. *Journal of Theoretical Biology*, 394:149–159.
- O’Dea, R. D., Byrne, H. M., and Waters, S. L. (2012). Continuum Modelling of In Vitro Tissue Engineering: A Review. In Geris, L., editor, *Computational Modeling in Tissue Engineering*, number 10 in Studies in Mechanobiology, Tissue Engineering and Biomaterials, pages 229–266. Springer Berlin Heidelberg.
- O’Dea, R. D., Nelson, M. R., El Haj, A. J., Waters, S. L., and Byrne, H. M. (2015). A multiscale analysis of nutrient transport and biological tissue growth in vitro. *Mathematical Medicine and Biology: A Journal of the IMA*, 32(3):345–366.
- O’Dea, R. D., Waters, S. L., and Byrne, H. M. (2010). A multiphase model for tissue construct growth in a perfusion bioreactor. *Mathematical Medicine and Biology: A Journal of the IMA*, 27(2):95–127.
- Pearson, N., Oliver, J., Shipley, R., and Waters, S. (2016a). A multiphase model for chemically- and mechanically- induced cell differentiation in a hollow fibre membrane bioreactor: minimising growth factor consumption. *Biomechanics and Modeling in Mechanobiology*, 15(3):683–700.
- Pearson, N., Shipley, R., Waters, S., and Oliver, J. (2016b). Dispersion-enhanced solute transport in a cell-seeded hollow fibre membrane bioreactor. *Journal of Engineering Mathematics*, 99(1):29–63.
- Pearson, N. C., Shipley, R. J., Waters, S. L., and Oliver, J. M. (2013). Multiphase modelling of the influence of fluid flow and chemical concentration on tissue growth in a hollow fibre membrane bioreactor. *Mathematical Medicine and Biology: A Journal of the IMA*, 31(4):393–430.

- Pearson, N. C., Waters, S., Oliver, J., and Shipley, R. (2015). Multiphase modelling of the effect of fluid shear stress on cell yield and distribution in a hollow fibre membrane bioreactor. *Biomechanics and Modeling in Mechanobiology*, 14(2):387–402.
- Penta, R., Ambrosi, D., and Shipley, R. J. (2014). Effective governing equations for poroelastic growing media. *The Quarterly Journal of Mechanics and Applied Mathematics*, 67(1):69–91.
- Pohlmeyer, J. V. and Cummings, L. J. (2013). Cyclic Loading of Growing Tissue in a Bioreactor: Mathematical Model and Asymptotic Analysis. *Bulletin of Mathematical Biology*, 75(12):2450–2473.
- Pohlmeyer, J. V., Waters, S. L., and Cummings, L. J. (2013). Mathematical Model of Growth Factor Driven Haptotaxis and Proliferation in a Tissue Engineering Scaffold. *Bulletin of Mathematical Biology*, 75(3):393–427.
- Riha, G. M., Lin, P. H., Lumsden, A. B., Yao, Q., and Chen, C. (2005). Roles of Hemodynamic Forces in Vascular Cell Differentiation. *Annals of Biomedical Engineering*, 33(6):772–779.
- Sahimi, M. (1993). Flow phenomena in rocks: from continuum models to fractals, percolation, cellular automata, and simulated annealing. *Reviews of Modern Physics*, 65(4):1393–1534.
- Sahimi, M. (1994). *Applications of percolation theory*. Taylor & Francis, London ; Bristol, PA.
- Shakeel, M., Matthews, P. C., Graham, R. S., and Waters, S. L. (2013). A continuum model of cell proliferation and nutrient transport in a perfusion bioreactor. *Mathematical Medicine and Biology: A Journal of the IMA*, 30(1):21–44.
- Shipley, R. J., Jones, G. W., Dyson, R. J., Sengers, B. G., Bailey, C. L., Catt, C. J., Please, C. P., and Malda, J. (2009). Design criteria for a printed tissue engineering construct: a mathematical homogenization approach. *Journal of Theoretical Biology*, 259(3):489–502.
- Thullner, M. and Baveye, P. (2008). Computational pore network modeling of the influence of biofilm permeability on bioclogging in porous media. *Biotechnology and bioengineering*, 99(6):1337–1351.
- Truscello, S., Kerckhofs, G., Van Bael, S., Pyka, G., Schrooten, J., and Van Oosterwyck, H. (2012). Prediction of permeability of regular scaffolds for skeletal tissue engineering: A combined computational and experimental study. *Acta Biomaterialia*, 8(4):1648–1658.
- Tsimpanogiannis, I. N. and Lichtner, P. C. (2012). Fluid Displacement and Solid Formation in a Porous Medium Using Invasion Percolation in a Gradient with Pore Blocking. *Energy & Fuels*, 26(6):3935–3950.
- Vafai, K. (2010). *Porous Media: Applications in Biological Systems and Biotechnology*. CRC Press, London.
- Van Blitterswijk, C. A. and Thomsen, P., editors (2008). *Tissue engineering*. Academic Press series in biomedical engineering. Elsevier, Acad. Press, Amsterdam.
- van Gennip, Y. and Bertozzi, A. L. (2012). Γ -convergence of graph Ginzburg-Landau functionals. *Advances in Differential Equations*, 17(11/12):1115–1180.

Whittaker, R. J., Booth, R., Dyson, R., Bailey, C., Chini, L. P., Naire, S., Payvandi, S., Rong, Z., Woollard, H., Cummings, L. J., Waters, S. L., Mawasse, L., Chaudhuri, J. B., Ellis, M. J., Michael, V., Kuiper, N. J., and Cartmell, S. (2009). Mathematical modelling of fibre-enhanced perfusion inside a tissue-engineering bioreactor. *Journal of Theoretical Biology*, 256(4):533–46.